Pure and Applied Geophysics

On the Monitoring of Small Islands Belonging to the Aeolian Archipelago by MT-InSAR Data

Marco Polcari,[1] Mimmo Palano,[2,3] Silvia Puliero,[1] Francesca Silverii,[1] Claudia Spinetti,[1] and Cristiano Tolomei[1]

Abstract—The aim of the present work is to evaluate the performance of several MT-InSAR techniques based on satellite SAR data in monitoring ground deformation phenomena affecting complex scenarios such as small islands of volcanic origin. To such purpose, PS, SBAS and IPTA approaches are applied in the study of Lipari, Salina and Vulcano islands belonging to the Aeolian archipelago, southern Tyrrhenian Sea, Italy. The outcomes retrieved from each technique are then discussed in terms of intrinsic features, spatial coverage, linear trend and coherence. Moreover, the accuracy of PS, SBAS and IPTA results are evaluated by comparison with in-situ measurements from the GNSS network managed by INGV-OE and private operators considering different metrics. Experimental results show that in this case there is no preferred MT-InSAR technique in an absolute way but each of them has strengths and drawbacks that have to be taken into account in the monitoring of complex scenarios.

Keywords: PS, SBAS, IPTA, aeolian archipelago, vulcano, GNSS.

1. Introduction

The monitoring of ground deformation of small islands by means of satellite Synthetic Aperture Radar Interferometry (InSAR) technique is typically quite challenging. Indeed, depending on the spatial resolution of SAR sensors, ranging from about 2–3 to 15–20 m, a few number of point targets could be found due to the small size of the islands and/or the presence of large vegetated areas resulting in temporal decorrelation phenomena. Moreover, the results can also be affected by atmospheric artifacts, water vapor effects and orbital errors caused by the surrounding sea and the complex topography, especially characterizing volcanic islands as the ones belonging to the Aeolian archipelago. This consists of seven major islands formed in the last 1.3 Ma in the framework of the active subduction of the Ionian domain beneath the Calabrian Arc (Barberi et al., 1973; Ventura et al., 1999). Overall, the subaerial volcanoes, along with a set of volcanic seamounts, form a ring-shaped-like structure bordering the abyssal plain around the Marsili seamount (Fig. 1). The three largest islands of the archipelago, i.e. Salina, Lipari and Vulcano, form a NNW-SSE-striking volcanic belt, which departs from the Aeolian ring-shaped structure. These islands along with the associated submarine eruptive centers developed along a NNW-SSE to NW–SE-trending regional structure, defined in literature as the Aeolian-Tindari-Letojanni fault, i.e. a seismically active and locally fragmented right-lateral fault system, extending from the Aeolian Islands down to the Ionian coast, north of Mt. Etna (Palano et al., 2015).

Because of the complexity of the scenario, very few studies applied remote sensing InSAR data for monitoring the Aeolian archipelago. Some of them focused on Stromboli island, which is one of the most active volcanoes in the world thus being of great interest for the scientific community. Di Traglia et al. (2018) and Schaefer et al. (2019) exploited SAR data acquired by Cosmo-SkyMed and Sentinel-1 missions to monitor the instability of the flank of Stromboli volcano known as Sciara del Fuoco. Di Traglia et al. (2014); (2021) proposed the synergistic use of both space-born and ground-based InSAR data for volcano monitoring and applied such approach to Stromboli island. Baldi et al. (2002) compared different

[1]   Istituto Nazionale di Geofisica e Vulcanologia, Osservatorio Nazionale Terremoti, Via di Vigna Murata 605, Rome, Italy. E-mail: marco.polcari@ingv.it
[2]   Department of Earth and Marine Sciences, University of Palermo, Via Archirafi 22, 90123 Palermo, Italy.
[3]   Istituto Nazionale di Geofisica e Vulcanologia, Osservatorio Etneo, Piazza Roma, 2, 95125 Catania, Catania, Italy.
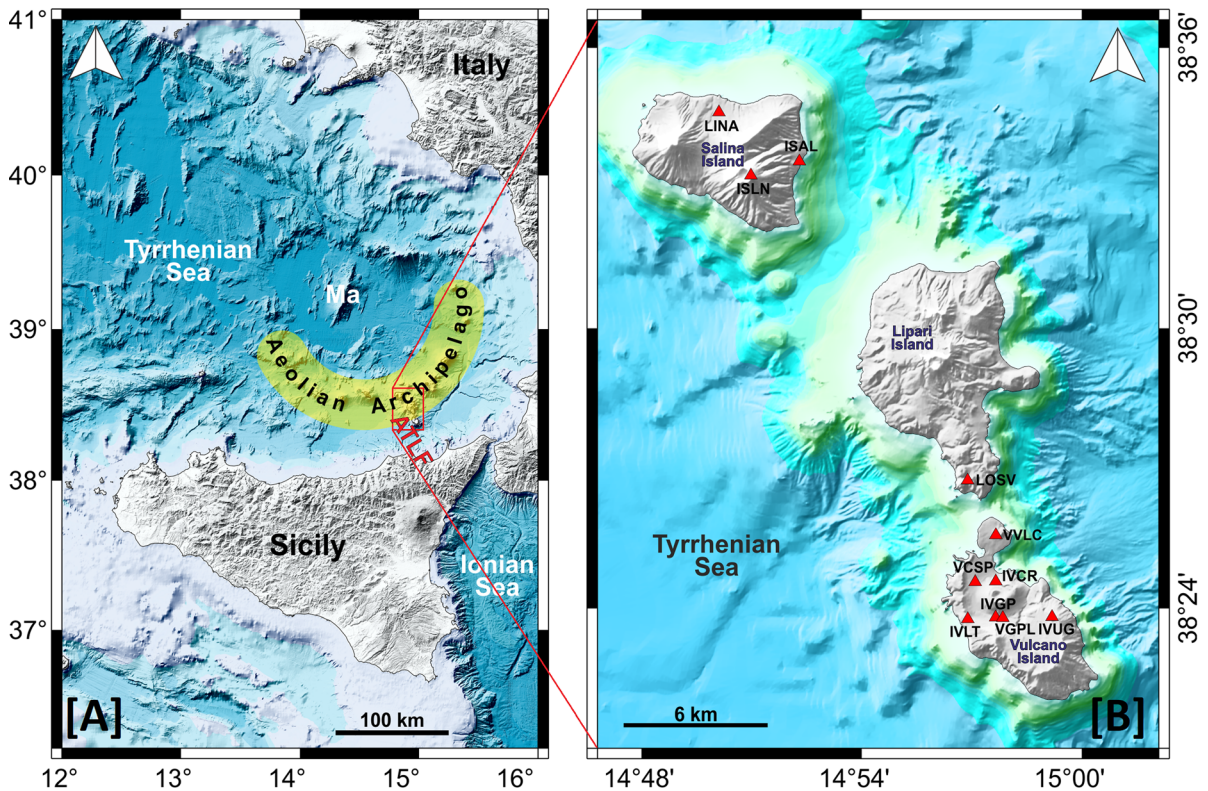
Figure 1

A Overview of southern Italy. ATLF, Aeolian-Tindari-Letojanni fault; Ma, Marsili Vulcano. **B** Zoom on the three islands of the Aeolian archipelago considered in this work (red rectangle-bounded area in (**A**)). The red triangles represent the GNSS continuous stations

techniques including InSAR to estimate the Digital Elevation Model (DEM) of Vulcano Island. Most recently, Di Traglia et al. (2023) exploited Sentinel-1 data to estimate and model the volcanic source responsible for the 2021 Vulcano island crisis.

The present work aims to analyze the performance of several Multi-Temporal InSAR (MT-InSAR) techniques for constraining any ground deformation phenomena affecting the largest islands of the Aeolian archipelago, i.e. Lipari, Salina, and Vulcano (Fig. 1). In particular, the outcomes from Persistent Scatterers (PS) (Ferretti et al., 2001), Small Baseline Subsets (SBAS) (Berardino et al., 2002) and Interferometric Point Target Analysis (IPTA) (Werner et al., 2003) algorithms are compared and cross-validated. The differences in terms of intrinsic features, spatial coverage, density of point targets and accuracy of the measurements are evaluated and discussed to point out strengths and drawbacks of

each of the three applied techniques. Moreover, to evaluate reliability and accuracy of the retrieved ground displacement time series, ground-truth data provided by the Global Navigation Satellite Sytem (GNSS) continuous stations managed by the Osservatorio Etneo of Istituto Nazionale di Geofisica e Vulcanologia (INGV-OE) and by private operators (e.g. Netgeo) are exploited. They consist of 11 stations located in Salina (3 stations), Lipari (1 station) and Vulcano (7 stations) and their daily measurements are used to validate the MT-InSAR results from the different techniques.

2. Method

InSAR is a remote sensing technique able to detect ground deformation patterns with accuracy in the order of mm/yr using satellite images acquired by

SAR sensors. In the original formulation, it exploits the phase difference between two SAR images acquired in different times, also called interferogram, to estimate the surface deformation along the satellite Line-of-Sight (LoS) due to natural or anthropogenic phenomena (Massonnet et al., 1993). In addition to the phase contribution due to any displacement fields, an interferogram is also composed by other contributions and can be summarized as follows:

$$\varphi = \varphi_{Disp} + \varphi_{Topo} + \varphi_{Atm} + \varphi_{Noise} \qquad (1)$$

where φ_{disp} is the contribution of interest, φ_{Topo} is the contribution due to the topography which can be removed either using an external DEM (e.g., Massonnet et al., 1993) or using a second SAR image pair (e.g., Zebker et al., 1994), φ_{Atm} is the phase due to any atmospheric artifacts and φ_{Noise} includes all the other noise contributions such as residual orbits, unwrapping errors, and decorrelation effects.

Advanced techniques based on the use of long multi-temporal datasets, i.e. MT-InSAR, have also been developed to fully exploit the potential offered by the nowadays huge amount of SAR images acquired by several space missions and to follow the temporal evolution of a deformation phenomenon significantly reducing the error contributions.

The existing algorithms mainly fall into two broad categories, namely PS (Ferretti et al., 2001) and SBAS (Berardino et al., 2002) approaches, with some algorithms exploiting the basic principles of both methodologies such as IPTA (Werner et al., 2003), SqueeSAR (Ferretti et al., 2011) and combined MT-InSAR method (Hooper et al., 2008).

The outputs of such techniques consist of linear velocity rate and ground displacement time-series, temporally referred to the first acquisition date of the image stack, and spatially referred to a point or areas within the radar coverage, with a millimeter accuracy of the retrieved measurements.

The PS-like methods aim to identify coherent radar targets exhibiting a high phase stability over the whole temporal span of the observations. These targets are only slightly affected by errors and decorrelation effects and often correspond to man-made structures or bare rocks. In the case of SBAS-like approaches, the interferometric pairs are chosen to minimize temporal and geometric decorrelation,

allowing to retrieve deformation time series for distributed scatterers, i.e., neighboring radar resolution cells, which are not dominated by a single scatterer, and share the same backscattering properties.

2.1. PS

PS technique exploits long datasets of full-resolution SAR images to identify those point targets characterized by low phase dispersion over the whole temporal span of the observations by taking into account several features of the interferometric phase components. Such points often correspond to man-made structures or bare rocks commonly referred to as Permanent Scatterers since they are only slightly affected by errors and decorrelation effects allowing a precise estimation of all the contributions of the interferometric phase. In particular, let N be the dimension of a SAR dataset, PS estimates N–1 interferograms generated with respect to the same master image chosen as reference. To mitigate the decorrelation effects, it is possible to rule out the interferometric pairs characterized by long spatial and/or temporal baselines and choose only the highly correlated pairs for subsequent interferometric analyses. The PS candidates are chosen according to a selected amplitude dispersion index threshold. Then, the retrieved points allow us to estimate and remove both the atmospheric and the residual orbital contributions and to estimate the ground displacement time series.

It has been pointed out that the computational burden in PS technique is quite high since it works with full-resolution data. In addition, the density of PS can be well-preserved only in urban areas whereas in areas with rare human activities, it can be less than 10 PS/km2 (Ferretti et al., 2011).

2.2. SBAS

The original SBAS technique works with datasets of multi-looked SAR images although full-resolution approaches have been also developed (Lanari et al., 2004). In the original version, the targets are represented by the so-called Distributed Scatterers (DS), i.e., neighboring radar resolution cells, which are not dominated by a single scatterer, and share the same

backscattering properties. Moreover, the interfero-metric pairs are grouped in several subsets characterized by small spatial and temporal baselines to minimize errors and decorrelation effects. Considering N SAR images, the interferograms network can span between N/2 and N(N–1)/2 according to the constraints imposed on the spatial and temporal baselines. Then, the interferograms are filtered and unwrapped and the ground displacement time series for each DS are reconstructed by an inversion algorithm, namely Single Value Decomposition (SVD). Along this step, the atmospheric contribution is estimated and removed, adopting double filtering in time and space. The capability of SBAS to work with multi-looked data and with small baseline results in a lower computational burden, and a greater spatial coverage but a worse resolution of the output products than PS technique.

2.3. IPTA

IPTA technique has been developed in the framework of GAMMA software (Wegmuller & Werner, 1997). It merges the main characteristics of PS and SBAS techniques working with both full-resolution and multi-looked data and can consider both single-master and multi-baseline approaches. Useful and noisy interferometric phase contributions such as deformations, orbital errors, and atmospheric artifacts are estimated and improved by an iterative approach. Point targets can be selected by spectral coherence criteria, intensity criteria, and sampling the multi-looked interferograms with regular grids. Moreover, it works on vector data thus significantly reducing both computational burden and data storage.

3. Sar Data & Processing

The considered SAR dataset consist of C-band Sentinel-1A images acquired in the TOPSAR mode from January 2016 to December 2023 along descending orbit with a revisit time of 12 days. The geometry of view is characterized by an incidence angle of about 39° and an azimuth angle of about 12°. The 30 m Digital Elevation Model (DEM) provided by the Shuttle Radar Topography Mission (SRTM)

was exploited to remove the topographic phase from the interferograms. In this work, all three aforementioned techniques have been applied by considering standard approaches, i.e., using default parameters suggested for most applications and can be theoretically performed also by non-expert users via online services or platforms. Full-resolution data exploited for PS approach are characterized by a pixel spacing of about 3.5 by 15 m along the range and azimuth direction. Following the single-master interferogram network generation (Fig. 2A), the image coregistration and the removal of the topographic phase contribution were carried out in the PS processing chain to estimate the interferograms. During the first inversion, the area of interest was divided into sub-areas of $25km^2$ with a 30% overlap. For each sub area, the most stable PS candidates were identified using the Amplitude Dispersion Index with a threshold of 0.7. These candidates are required to apply a linear model to estimate residual height and displacement velocity. Afterward, in the second inversion, high and low pass filters were applied to perform atmospheric corrections and determine the final displacement and mean velocity.

The multi-looked interferograms used in SBAS and, partially, in IPTA techniques are obtained by applying multilooking factors of 8 by 2 along range and azimuth direction, respectively resulting in a ground pixel resolution of about 30 m. The interferogram networks are obtained considering constraints for perpendicular and temporal baseline such to obtain dense networks (Fig. 2B, C). In particular, a maximum perpendicular baseline of 110 m and a time gap ranging between 12 and 180 days were considered for SBAS approach. On the other hand, for IPTA approach a maximum of 5 connections for each images have been set starting from 36 days. Goldstein filtering (Goldstein & Werner, 1998) was applied to all the interferograms and then they were unwrapped through the Minimum Cost Flow algorithm (Costantini, 1998). Then, for the SBAS approach, the stack of the interferometric pairs is inverted using the Single Value Decomposition (SVD) method to obtain the displacement time series for each coherent pixel considering a linear model for the motion. At this step, a double filtering in the space and time (high and low pass filter) domain is
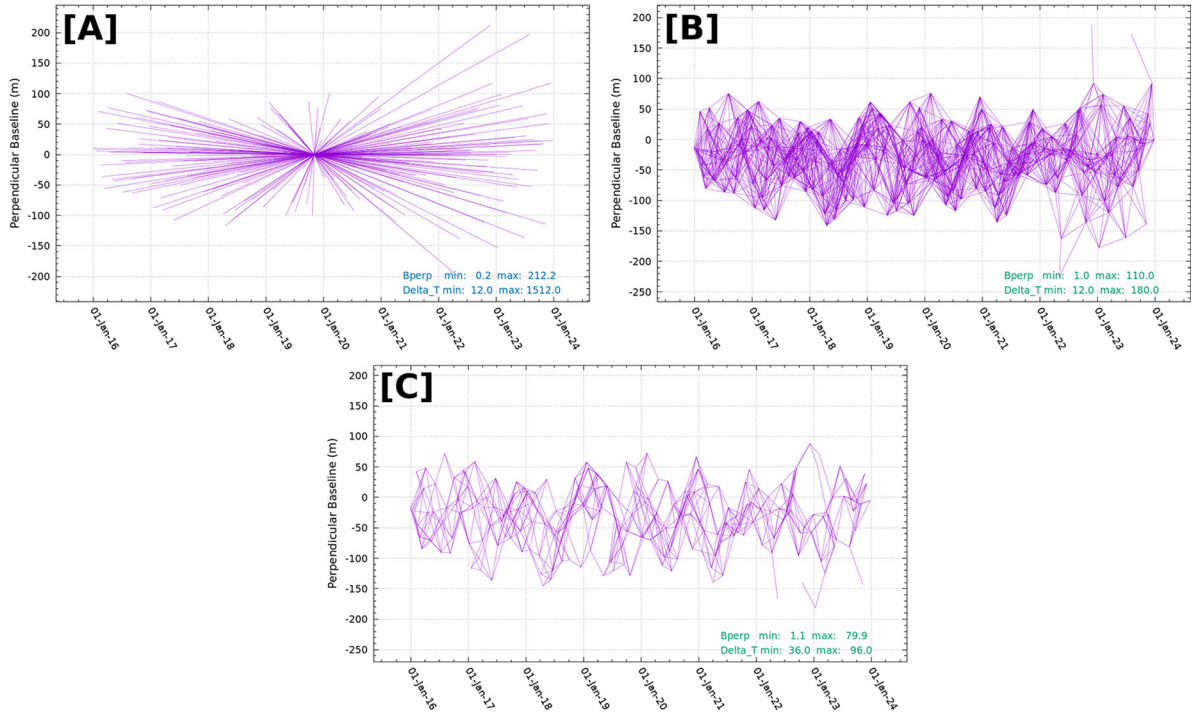
Figure 2
Interferogram networks generated for PS [**A**], SBAS [**B**] and IPTA [**C**] techniques

performed to estimate and remove the atmospheric contribution. Finally, the regression trend is computed for each time series providing the mean velocity value.

In the case of the IPTA processing, the point targets were first selected by both spectral coherence and intensity criteria setting the threshold to 0.3 and 0.75, respectively. In addition, a regular grid was also considered, by using a step of 60 m, to sample and include the multi-looked estimated interferograms. All the point targets were masked according to the estimated layover, shadow, and very low coherence areas. The final solution in terms of displacement time series and linear velocity was then found by an extension of the Singular Value Decomposition (SVD) based Least-Squares inversion (Werner et al., 2012).

4. GNSS Data and Processing

All GNSS observations collected since 2016 by the continuous stations installed over the study area were processed with the GAMIT/GLOBK software packages (Herring et al., 2018). The overall processing was performed by adopting the strategy described in Chiarabba and Palano (2017). To tie the regional measurements to an external global reference frame, we included in the processing the raw data coming from about 25 continuously operating stations (e.g., https:/igs.org, https:/epncb.oma.be/). By using the GLOBK package (Herring et al., 2018) we combined the GAMIT solutions to estimate, on a daily basis, a consistent set of time-series positions aligned to a local reference frame (Cintorrino et al., 2019). Achieved time series have been projected in the Satellite LoS (Fig. 6) in order to compare them with the time series retrieved with the three InSAR techniques mentioned above (i.e., PS, SBAS and IPTA).

5. Results

The results of the three approaches are shown in Fig. 3. The mean ground deformation velocity estimated using the different techniques shows, over the

investigated time interval, a clear deformation pattern affecting the main crater of Vulcano island, called La Fossa, and general stability in the other two islands with few localized deformation phenomena detected in Lipari and Salina likely due to landslide processes.

La Fossa crater is indeed characterized by a long-term subsidence trend mainly due to shallow geothermal processes (Alparone et al., 2019; Gambino & Guglielmino, 2008) and/or to the contraction of a magmatic source located at a depth of $\sim$ 4 km (Cintorrino et al., 2019). However, starting from July 2021, this sector of Vulcano was affected by an important crisis with variations of several parameters such as gas emissions, thermal anomalies, and since early September 2021 by a marked uplift peaking at about 30 mm detected along the central part of the crater in November 2021 (Di Traglia et al., 2023;

Federico et al., 2023; Rabuffi et al., 2022; Stissi et al., 2023). Such a spatial pattern is clearly visible in Fig. 4, while in Fig. 5 the time series averaged from several points located in the area of maximum deformation showing a marked variation since mid-September 2021 are reported. The investigation on the causative source of the 2021 unrest of Vulcano is out of the main scope of this work, however various hypotheses have been proposed in recent literature. For instance, Aiuppa et al. (2022), by analyzing a set of geochemical data, suggested that the unrest was driven by a batch of mafic magma emplaced at about 5 km depth, while Federico et al. (2023) by using a similar set of data, suggested a deep-seated change in the plumbing system of Vulcano. Di Traglia et al. (2023) used a combined approach of geodetic, satellite and seismic data to instead propose a
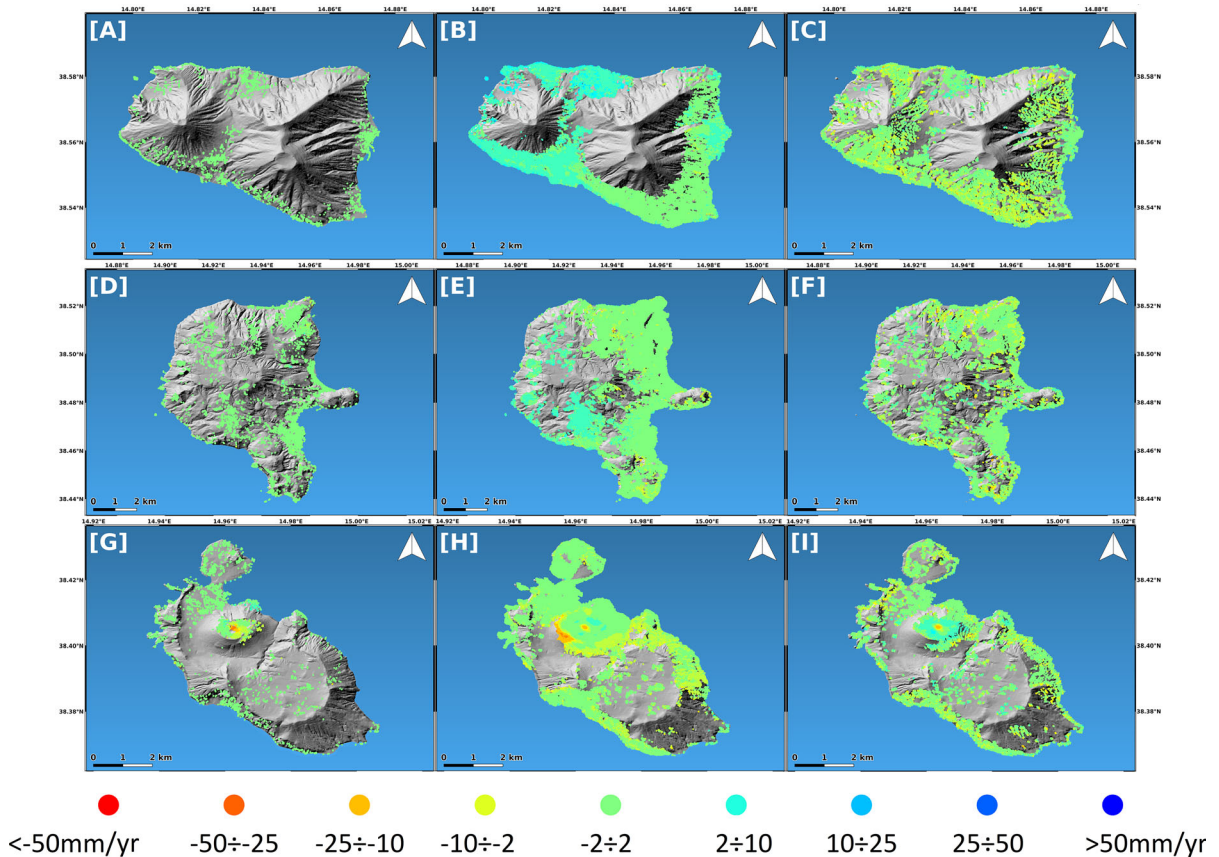

Figure 3
LoS Deformation rate retrieved for Salina, Lipari and Vulcano islands respectively by PS [**A**, **D**, **G**], SBAS [**B**, **E**, **H**] and IPTA [**C**, **F**, **I**] techniques. The background image is the 10 m resolution Tinitaly DEM (Tarquini et al., 2023)
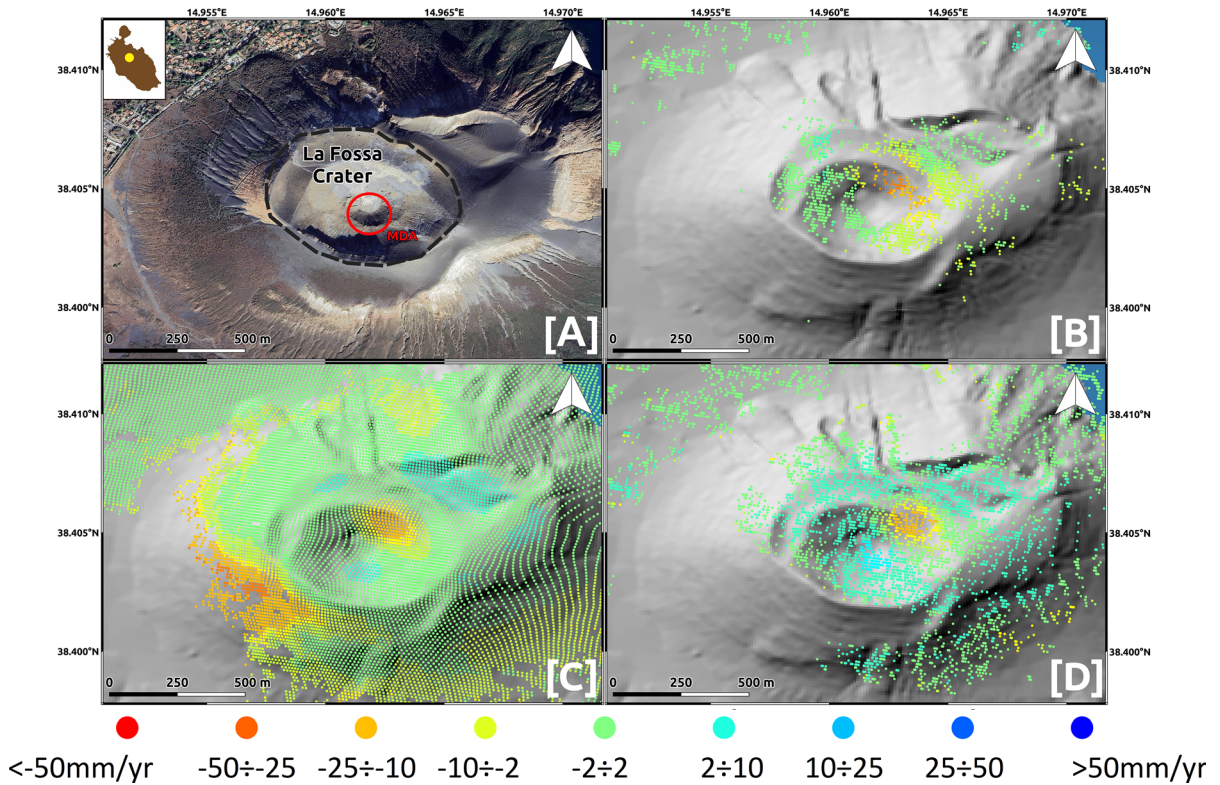
Figure 4

Focus on La Fossa crater in Vulcano island. The crater is indicated with the dashed black polygon in [A] whereas the red circle represents the Maximum Deformation Area (MDA) during the 2021 crisis. Outcomes in terms of ground deformation velocity from PS [B], SBAS [C] and IPTA [D]

hydrothermally-driven unrest. Stissi et al. (2023) reached similar considerations by using geodetic data.

Both the quasi-linear pre-crisis subsidence and the 2021 uplift is well constrained by SBAS and IPTA approaches which are consistent with each other for behavior and intensity of the pattern. On the other hand, PS shares the same behavior but with a lower intensity of the deformation values. This is most likely due to the lack of points in the Maximum Deformation Area (MDA).

Table 1 summarizes several parameters estimated for each of the three islands to evaluate the performances of the applied approaches. SBAS provides the higher density of points in all the islands with about 70%, 79%, and 84% of points more than PS for Lipari, Vulcano, and Salina islands and about 36%, 39%, and 3% of points more than IPTA for Lipari, Vulcano, and Salina island, respectively. The Root

Mean Square Error (RMSE) values associated with the linear trend and the coherence are quite similar for SBAS and IPTA with the first slightly overper-forming for Lipari and Vulcano island. Instead, for Salina Island, the mean coherence retrieved by SBAS approach is equal to 0.23, which is 0.12 smaller than the coherence value calculated using the IPTA approach. On the other hand, PS shows a higher mean coherence spanning from 0.77 to 0.78 with a clear lower dispersion. It is quite obvious that the draw-back is the low spatial coverage since PS only considers points characterized by backscattering properties stable along the entire dataset such as roads, buildings, and rocks that show high coherence values but are not so many.

The RMSE of the PS method also overperforms both SBAS and IPTA approaches of about 30–40% indicating how PS tends to flatten the observed phenomena.
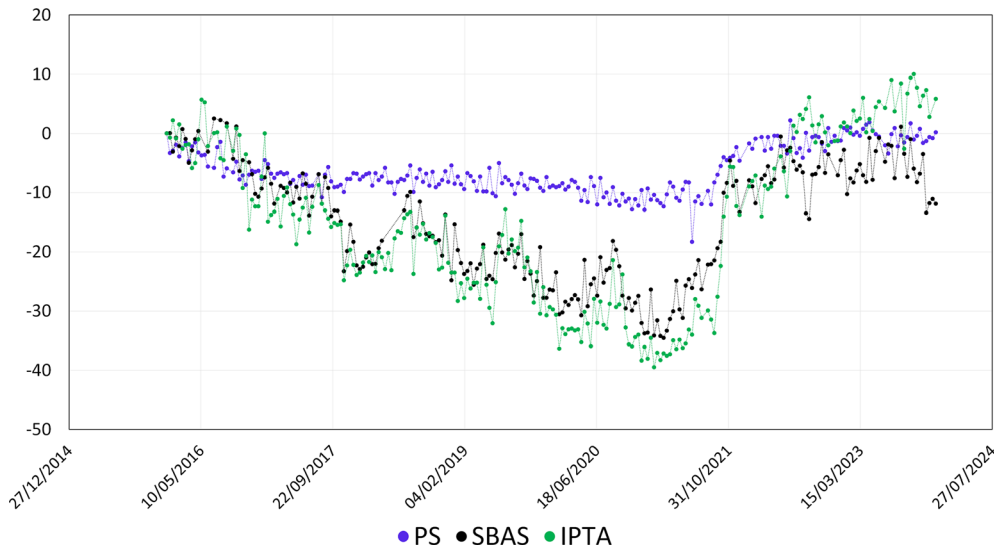
Figure 5
LoS displacement time series averaged from the point targets located in the MDA represented as the red circle in Fig. 4a. The measurements are expressed in mm

Table 1

Overview on the performances of the three MT-InSAR techniques applied in this work

	Island	Number of points	RMSE with respect linear trend [mm]	Mean coherence	Coherence st.dev
PS	Lipari	19,518	2.86	0.78	0.06
	Vulcano	9129	2.96	0.77	0.05
	Salina	6207	2.99	0.77	0.05
SBAS	Lipari	64,420	4.09	0.44	0.14
	Vulcano	42,456	4.24	0.46	0.17
	Salina	37,390	5.10	0.23	0.07
IPTA	Lipari	41,112	4.95	0.39	0.14
	Vulcano	25,856	4.98	0.40	0.14
	Salina	36,326	5.03	0.35	0.09

In order to evaluate the accuracy of the measurements, the time series retrieved with the three techniques are compared with the LoS-projected GNSS measurements of the continuous stations installed on the islands (Fig. 6). All the measurements of InSAR points inside a circle centered on the GNSS station with a radius of 200 m are averaged and used for the comparison.

Between the available GNSS sites, VGPL, located in the proximity of La Fossa crater, is not used since

it does not cover the time interval considered for MT-InSAR techniques, whereas IVUG (in Vulcano island) and ISLN (in Salina islands) are not shown because of the lack of PS, SBAS and IPTA point targets in the surroundings of the stations. The station called ISAL, located in Santa Maria Salina village, is used as a reference for a relative reference system since it is characterized by a long time series entirely covering the MT-InSAR time interval and, neglecting the long-term tectonic movements, it does not show any significant deformations.

In order to quantitatively estimate the comparison between GNSS and InSAR time series, we first applied a Gaussian filter with standard deviation of 90 days, in order to remove the high-frequency (daily-to-monthly) oscillations, and we resampled the GNSS time series at 12-days rate. Figure 7, panel A, shows an example of the outcome for site VCSP. Afterwards, we computed the residuals between each MT-InSAR time series and the corresponding GNSS one (Fig. 7, panel B) and we estimated the misfit as RMSE, Mean Absolute Error (MAE) and correlation coefficient R^2 (Table 2). Both RMSE and MAE metrics are sensitive to the values of the two time series to be compared and are expressed in mm, whereas R^2 is a normalized parameter ranging
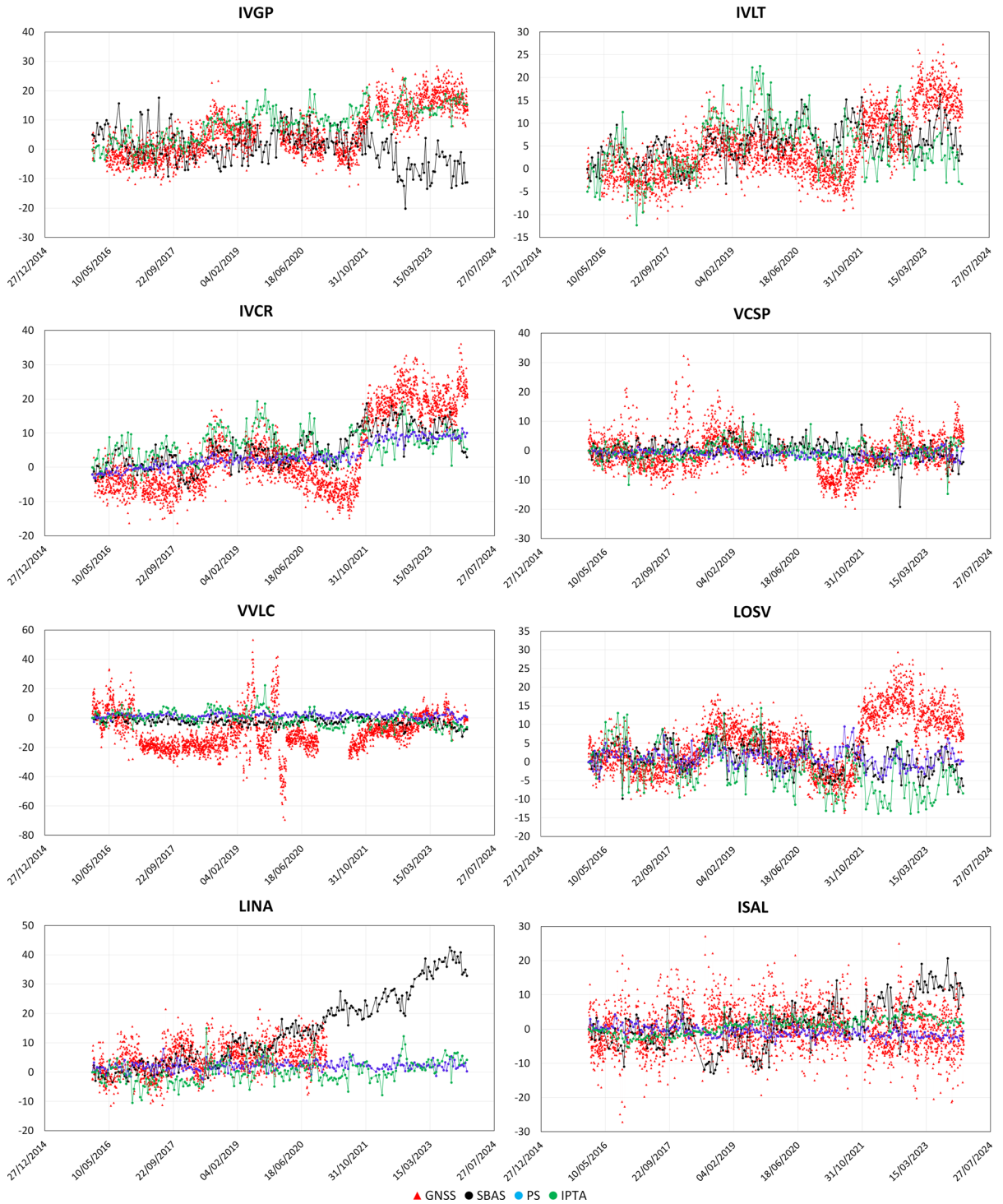
Figure 6
Comparison between LoS displacement time series from GNSS (red), PS (blue), SBAS (black) and IPTA (green). The measurements are expressed in mm
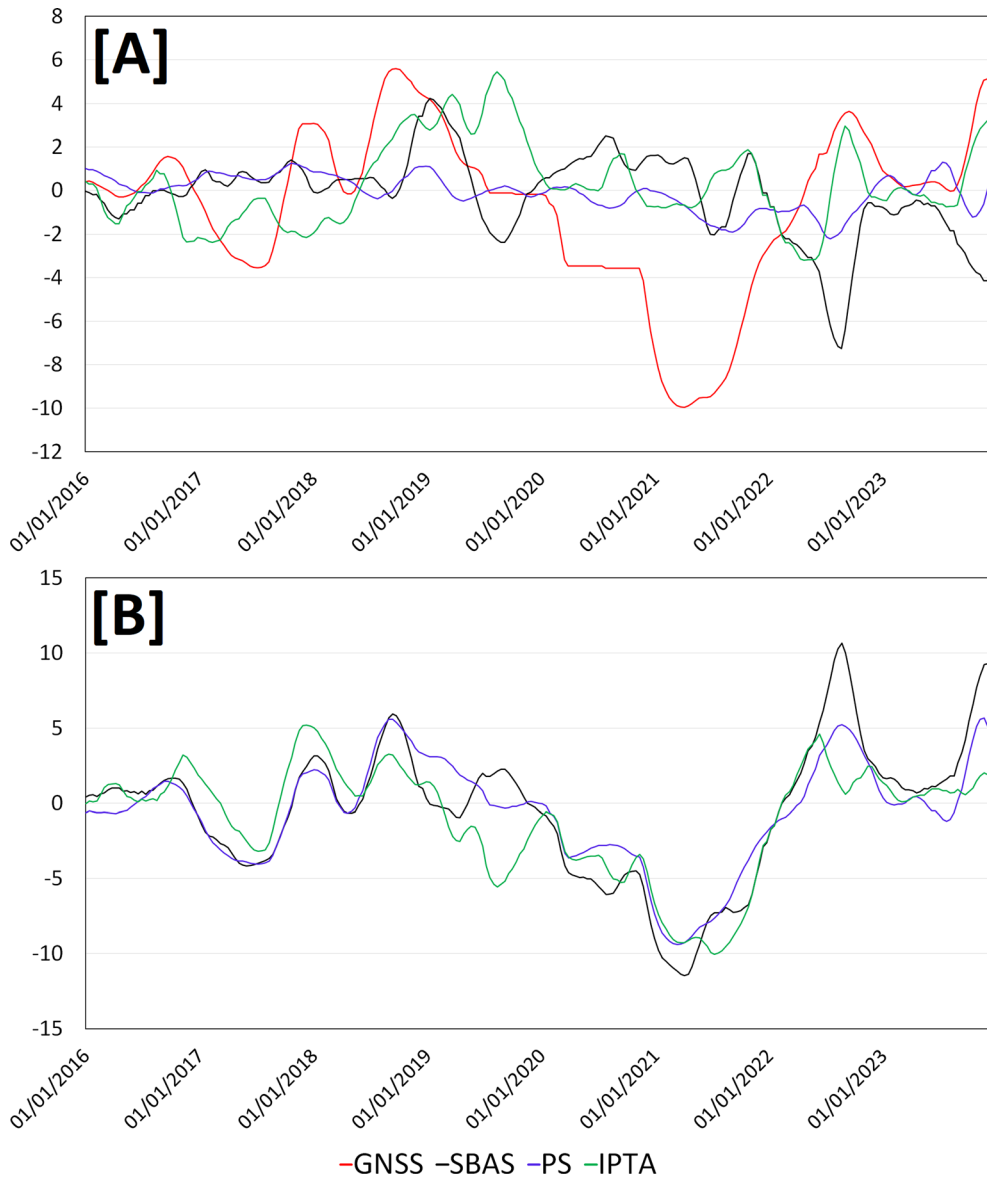
Figure 7
Best-fitting functions of GNSS and InSAR measurements used for the evalutation of RMSE, MAE and R^2 (**A**) and related residuals (**B**) for the VCSP station. The measurements are expressed in mm

between 0 and 1 and takes into account only the shape of the two time series.

6. Discussion and Conclusions

The comparison of the performance of the MT-InSAR technique applied in the present study allows to provide general considerations about the monitoring of small-to-medium islands by satellite data. The SBAS approach can provide a considerable number of point targets returning a better spatial coverage and more measurement points in areas where the other techniques are not able to retrieve any points, at least using default parameters. However, in some cases, including more points could not guarantee reliable

Table 2

Overview on the performance of InSAR techniques considering different metrics with respect to GNSS measurements

Station	Metric	SBAS	PS	IPTA
IVCR	RMSE	7.09	7.11	9.33
IVCR	MAE	5.65	5.66	6.67
IVCR	R^2	0.60	0.83	0.23
IVGP	RMSE	10.56	NA	4.51
IVGP	MAE	8.18	NA	3.67
IVGP	R^2	0.51	NA	0.62
IVLT	RMSE	5.39	NA	7.09
IVLT	MAE	4.19	NA	5.69
IVLT	R^2	0.16	NA	0.02
LINA	RMSE	4.94	2.56	2.91
LINA	MAE	3.68	1.96	2.32
LINA	R^2	0.39	0.22	0.17
LOSV	RMSE	7.04	6.98	8.88
LOSV	MAE	5.56	5.70	7.26
LOSV	R^2	0.01	0.14	0.08
VCSP	RMSE	4.55	3.54	3.80
VCSP	MAE	3.42	2.64	2.83
VCSP	R^2	0.04	0.12	0.07
VVLC	RMSE	8.94	8.51	9.61
VVLC	MAE	7.97	7.57	8.20
VVLC	R^2	0.09	0.04	0.01
ISAL	RMSE	7.02	2.15	2.58
ISAL	MAE	5.09	1.67	2.14
ISAL	R^2	0.09	0.01	0.01

RMSE and MAE are expressed in mm whereas R^2 is dimensionless

results. Indeed, for Salina island, the mean coherence is quite low and the validation with the GNSS LINA and ISAL stations shows a significant disagreement (Fig. 6). Such weak performances are probably due to the use of several distributed scatterers largely affected by several errors due to atmospheric artifacts, unwrapping errors or orbital errors. The same occurs for IVGP station where SBAS show the worst performance of the dataset in terms of RMSE (10.56 mm) and MAE (8.18 mm). On the other hand, PS can detect local deformation phenomena in the order of a few meters since it works with full resolution SAR images. Moreover, it is less affected by unwrapping errors and shows the best performance in terms of all the three metrics (RMSE, MAE and R^2) for almost all the stations. The main drawback is related to the general lack of points outside urban areas which prevents the complete characterization of several natural phenomena as in the case of the 2021 Vulcano crisis where no point targets have been

found in the maximum deformation area nor in the proximity of IVGP and IVLT stations. This issue can be theoretically improved by using lower thresholds for the point target candidate selection but this would also add further errors which are instead mitigated with multi-looked approaches. In addition, PS derived time series are more smoothed around the linear trend, as observed in Fig. 6 for most of the stations, and this can be a drawback when dealing with non-linear deformation phenomena. IPTA merges the main features of the two approaches working with both full resolution and multi-looked data and provides a better spatial coverage than PS and a lower sensitivity to data or processing errors than SBAS, at least for Salina island. However, the selection of multi-looked point targets is not always led by strict criteria and this can affect the quality of the results. Indeed, IPTA shows the worst mean coherence for Lipari (0.39) and Vulcano (0.40) and also for Salina the mean coherence is quite low being equal to 0.35 although greater than SBAS. Also the performance of the three metrics are not particularly satisfactory for IVCR, IVLT, LOSV and VVLC (Table 1). Instead for IVGP, LINA, ISAL and VCSP the agreement between GNSS and IPTA measurements is quite good (Fig. 6) and the performances of RMSE, MAE and R^2 are close to PS. Concerning hardware and software required by the three technique, PS and SBAS processing were performed by using the SARscape software 5.7.0, developed by sarmap SA [©] 2022, which is included in the ENVI 5.7 package (NV5[™]). The workstation used to run the processing was a Lenovo ThinkStation P340 with an Intel(R) Core(TM) i9-10,900 CPU @ 2.80 GHz, 2.81 GHz, GPU NVIDIA Cuda Quadro P620, and 64 GB RAM in a Windows 11 Pro environment. On the other hand, IPTA processing was performed by exploiting the GAMMA software of the GAMMA Remote Sensing [©]. It is originally developed and optimized to work on Linux environment then the processing was run using Ubuntu 20.04 LTS operative system mounted on a workstation DELL Thinkstation Intel(R) Xeon(R) CPU E5-2637 v3 @ 3.50 GHz and 64 GB RAM. High performing CPU and RAM are needed to manage the huge amount of data provided by Sentinel-1 mission and the similar features of the two workstation allow to provide an

indication about the computational costs required by the three technique. SBAS required the longer processing times of about 15 days because of the huge number of interferograms estimated. On the other hand, the multilooking step significantly reduced the memory needed to storage data and output products, which is about 1.10 TB. IPTA estimated a lower number of interferograms but also considering a limited number of full resolution data requiring a storage of about 1.32 TB. However, it mainly works with vector data format allowing to reduce the processing time to about 5 days. Finally, PS is the only working with all full resolution data and required a storage of about 1.52 TB and a processing time of about 9 days. In general, it is not possible to indicate one of the techniques as the best for the monitoring of small islands. All of them show strengths and drawbacks and are more or less suitable to be exploited according to the scale, the scenario and the intensity of the deformation phenomenon to be studied. Certainly, the default parameters do not seem to be the most appropriate in many cases since on one hand they do not allow to retrieve enough point targets, as in the case of PS for the study of 2021 Vulcano crisis, and on the other hand they return too much point likely affected by errors, such as the case for SBAS applied to Salina island. In this sense, the most important outcome of the present study is that under some conditions, MT-InSAR techniques cannot be considered user-friendly and performed as totally automatic procedures. Indeed, an expert user is required to modify and adapt some processing parameters according to the features of scenario and phenomenon to analyze in order to improve reliability and accuracy of the results.

Data Availability

The data are available on request.

Declarations

Publisher's Note Springer Nature remains neutral with regard to jurisdictional claims in published maps and institutional affiliations.

REFERENCES

Aiuppa, A., Bitetto, M., Calabrese, S. Delle., Donne, D., Lages, J., La Monica, F. P., Chiodini, G., Tamburello, G., Cotterill, A., Fulignati, P., Gioncada, A., Liu, E. J., Moretti, R., & Pistolesi, M. (2022). Mafic magma feeds degassing unrest at Vulcano Island. *Italy. Communications Earth & Environment, 3*, 255. https://doi.org/10.1038/s43247-022-00589-1

Alparone, A., Bonforte, A., Gambino, S., Guglielmino, F., Obrizzo, F., & Velardita, R. (2019). Dynamics of Vulcano Island (Tyrrhenian Sea, Italy) investigated by long-term (40 years)

geophysical data. *Earth-Science Reviews, 190*, 521–535. https://doi.org/10.1016/j.earscirev.2019.01.002

Baldi, P., Bonvalot, S., Briole, P., Coltelli, M., Gwinner, K., Marsella, M., Puglisi, G., & Rémy, D. (2002). Validation and comparison of different techniques for the derivation of digital elevation models and volcanic monitoring (Vulcano Island, Italy). *International Journal of Remote Sensing, 23*(22), 4783–4800. https://doi.org/10.1080/01431160110115861

Barberi, F., Gasparini, P., Innocenti, F., & Villari, L. (1973). Volcanism of the Southern Tyrrhenian Sea and its geodynamics implications. *Journal of Geophysical Research, 78*, 5221–5232. https://doi.org/10.1029/JB078i023p05221

Berardino, P., Fornaro, G., Lanari, R., & Sansosti, E. (2002). A new algorithm for surface deformation monitoring based on small baseline differential SAR interferograms. *IEEE Trans. Geosci. Remote Sens, 40*, 2375–2383. https://doi.org/10.1109/TGRS.2002.803792

Chiarabba, C., & Palano, M. (2017). Progressive migration of slab break-off along the southern Tyrrhenian plate boundary: Constraints for the present day kinematics. *Journal of Geodynamics, 105*, 51–61. https://doi.org/10.1016/j.jog.2017.01.006

Cintorrino, A. A., Palano, M., & Viccaro, M. (2019). Magmatic and tectonic sources at Vulcano (Aeolian Islands, SouthernItaly): A geodetic model based on two decades of GPS observations. *Journal of Volcanology and Geothermal Research, 388*, 106689. https://doi.org/10.1016/j.volgeores.2019.106689

Costantini, M. (1998). A novel phase unwrapping method based on network programming. *IEEE Transactions on Geoscience and Remote Sensing, 36*, 813–821. https://doi.org/10.1109/36.673674

Di Traglia, F., Bruno, V., Casu, F., Cocina, O., De Luca, C., Giudicepietro, F., et al. (2023). Multi-temporal InSAR, GNSS and seismic measurements reveal the origin of the 2021 Vulcano Island (Italy) unrest. *Geophysical Research Letters, 50*, e2023GL104952. https://doi.org/10.1029/2023GL104952

Di Traglia, F., De Luca, C., Manzo, M., Nolesini, T., Casagli, N., Lanari, R., & Casu, F. (2021). Joint exploitation of space-borne and ground-based multitemporal InSAR measurements for volcano monitoring: The Stromboli volcano case study. *Remote Sensing of Environment, 260*, 0034–4257. https://doi.org/10.1016/j.rse.2021.112441

Di Traglia, F., Nolesini, T., Intrieri, E., Mugnai, F., Leva, D., Rosi, M., & Casagli, N. (2014). Review of ten years of volcano deformations recorded by the ground-based InSAR monitoring system at Stromboli volcano: a tool to mitigate volcano flank dynamics and intense volcanic activity. *Earth-Science Reviews, 139*, 317–335. https://doi.org/10.1016/j.earscirev.2014.09.011

Di Traglia, F., Nolesini, T., Solari, L., Ciampalini, A., Frodella, W., Steri, D., Allotta, B., Rindi, A., Marini, L., Monni, N., Galardi, E., & Casagli, N. (2018). Lava delta deformation as a proxy for submarine slope instability. *Earth and Planetary Science Letters, 488*, 46–58. https://doi.org/10.1016/j.epsl.2018.01.038

Federico, C., Cocina, O., Gambino, S., Paonita, A., Branca, S., Coltelli, M., Italiano, F., Bruno, V., Caltabiano, T., Camarda, M., et al. (2023). Inferences on the 2021 Ongoing Volcanic Unrest at Vulcano Island (Italy) through a Comprehensive Multidisciplinary Surveillance Network. *Remote Sensing, 15*, 1405. https://doi.org/10.3390/rs15051405

Ferretti, A., Fumagalli, A., Novali, F., Prati, C., Rocca, F., & Rucci, A. (2011). A new algorithm for processing interferometric datastacks: SqueeSAR. *IEEE Transactions on Geoscience and Remote Sensing, 49*, 3460–3470. https://doi.org/10.1109/TGRS.2011.2124465

Ferretti, A., Prati, C., & Rocca, F. (2001). Permanent scatterers in SAR interferometry. *IEEE Transactions on Geoscience and Remote Sensing, 39*(1), 8–20. https://doi.org/10.1109/36.898661

Gambino, S., & Guglielmino, F. (2008). Ground deformation induced by geothermal processes: A model for La Fossa Crater (Vulcano Island, Italy). *Journal of Geophysical Research, 113*, B07402. https://doi.org/10.1029/2007JB005016

Goldstein, R., & Werner, C. (1998). Radar interferogram filtering for geophysical applications. *Geophysical Research Letters, 25*, 4035–4038. https://doi.org/10.1029/1998GL900033

Herring, T.A., King, R., Floyd, M.A., McClusky, S.C. (2018). Introduction to GAMIT/ GLOBK, Release 10.7. Massachusetts Institute of Technology, Cambridge, UK. https :/www-gpsg.mit.edu.

Hooper, A. (2008). A multi-temporal InSAR method incorporating both persistent scatterer and small baseline approaches. *Geophysical Research Letters, 35*, L16302. https://doi.org/10.1029/2008GL034654

Lanari, R., Mora, O., Manunta, M., Mallorqui, J. J., Berardino, P., & Sansosti, E. (2004). A small-baseline approach for investigating deformations on full-resolution differential SAR interferograms. *IEEE Transactions on Geoscience and Remote Sensing, 42*(7), 1377–1386. https://doi.org/10.1109/TGRS.2004.828196

Massonnet, D., Rossi, M., Carmona, C., et al. (1993). The displacement field of the Landers earthquake mapped by radar interferometry. *Nature, 364*, 138–142. https://doi.org/10.1038/364138a0

Palano, M., Schiavone, D., Loddo, M., Neri, M., Presti, D., Quarto, R., Totaro, C., & Neri, G. (2015). Active upper crust deformation pattern along the southern edge of the Tyrrhenian subduction zone (NE Sicily): Insights from a multidisciplinary approach. *Tectonophysics, 657*, 205–218. https://doi.org/10.1016/j.tecto.2015.07.005

Rabuffi, F., Silvestri, M., Musacchio, M., Romaniello, V., & Buongiorno, M. F. (2022). A statistical approach to satellite time series analysis to detect changes in thermal activities: The Vulcano Island 2021 crisis. *Remote Sensing, 14*, 3933. https://doi.org/10.3390/rs14163933

Schaefer, L. N., Di Traglia, F., Chaussard, E., Lu, Z., Nolesini, T., & Casagli, N. (2019). Monitoring volcano slope instability with Synthetic Aperture Radar: A review and new data from Pacaya (Guatemala) and Stromboli (Italy) volcanoes. *Earth-Science Reviews, 192*, 236–257. https://doi.org/10.1016/j.earscirev.2019.03.009

Stissi, S. C., Currenti, G., Cannavò, F., & Napoli, R. (2023). Evidence of poro-elastic inflation at the onset of the 2021 Vulcano Island (Italy) unrest. *Frontiers in Earth Science, 11*, 1179095. https://doi.org/10.3389/feart.2023.1179095

Tarquini S., I. Isola, M. Favalli, A. Battistini, G. Dotta (2023). TINITALY, a digital elevation model of Italy with a 10 meters cell size (Version 1.1). Istituto Nazionale di Geofisica e Vulcanologia (INGV). https://doi.org/10.13127/tinitaly/1.1

Ventura, G., Vilardo, G., Milano, G., & Pino, N. A. (1999). Relationships among crustal structure, volcanism and strike–slip tectonics in the Lipari-Vulcano volcanic complex (Aeolian Islands, Southern Tyrrhenian Sea, Italy). *Physics of the Earth and Planetary Interiors, 116*(1–4), 31–52. https://doi.org/10.1016/S0031-9201(99)00117-X

Wegmuller, U., & Werner, C. (1997). Gamma SAR processor and interferometry software. *Proceedings of the ERS Symposium on Space at the Service of Our Environment, Florence, Italy, ESA Publications Division: Florence, Italy, 1997*, 1687–1692.

Werner, C.L., Wegmüller, U., Strozzi, T. (2012). Deformation time-series of the Lost-Hills oil field using a multi-baseline interferometric SAR inversion algorithm with finite difference smoothing constraints, in: AGU Fall Meeting Abstracts, pp. G43A–0910.

Werner, C., Wegmuller, U., Strozzi, T., & Wiesmann, A. (2003). Interferometric point target analysis for deformation mapping. *IEEE Int. Geosci. Remote Sens., 7*, 4362–4364. https://doi.org/10.1109/IGARSS.2003.1295516

Zebker, H. A., Werner, C. L., Rosen, P. A., & Hensley, S. (1994). Accuracy of topographic maps derived from ERS-1 interferometric radar. *IEEE Transactions on Geoscience and Remote Sensing, 32*(4), 823–836. https://doi.org/10.1109/36.298010